Real-time MRI-Guided Needle Placement Robot with Integrated Fiber Optic Force Sensing

Hao Su, Michael Zervas, Gregory A. Cole, Cosme Furlong, Gregory S. Fischer

Abstract— This paper presents the first prototype of a magnetic resonance imaging (MRI) compatible piezoelectric actuated robot integrated with a high-resolution fiber optic sensor for prostate brachytherapy with real-time *in situ* needle steering capability in 3T MRI. The 6-degrees-of-freedom (DOF) robot consists of a modular 3-DOF needle driver with fiducial tracking frame and a 3-DOF actuated Cartesian stage. The needle driver provides needle cannula rotation and translation (2-DOF) and stylet translation (1-DOF). The driver mimics the manual physician gesture by two point grasping. To render proprioception associated with prostate interventions, a Fabry-Perot interferometer based fiber optic strain sensor is designed to provide high-resolution axial needle insertion force measurement and is robust to large range of temperature variation. The paper explains the robot mechanism, controller design, optical modeling and opto-mechanical design of the force sensor. MRI compatibility of the robot is evaluated under 3T MRI using standard prostate imaging sequences and average signal noise ratio (SNR) loss is limited to 2% during actuator motion. A dynamic needle insertion is performed and bevel tip needle steering capability is demonstrated under continuous real-time MRI guidance, both with no visually identifiable interference during robot motion. Fiber optic sensor calibration validates the theoretical modeling with satisfactory sensing range and resolution for prostate intervention.

Keywords: Optical Force Sensor, Fabry-Perot Interferometer, MRI Compatibility, Needle Driver, Brachytherapy.

I. INTRODUCTION

Subcutaneous needle, catheter and electrode insertion is one of the most common minimally invasive procedures [1]. Needle placement error can be categorized as intrinsic and extrinsic ones. For intrinsic ones, needle deflection due to tissue-needle interaction causes the deviation of needle tip from the target. Intra- and post-operative edema induces implanted seed drift for procedures like brachytherapy. For extrinsic errors, perturbations are caused by patient movement, respiratory motion, and external surgical tool caused tissue deformation (e.g. ultrasound probe), etc. To compensate these errors is one of the major motivations of deploying active needle steering. The proposed needle driver is capable of steering bevel tip needle and active cannula while with a clinical application on prostate brachytherapy.

Early MRI-guided prostate robots focus on manual actuation. There is active work being developed in the area

H. Su, G.A. Cole and G.S. Fischer are with Automation and Interventional Medicine (AIM) Robotics Laboratory, Department of Mechanical Engineering, Worcester Polytechnic Institute, 100 Institute Road, Worcester, MA 01609, USA [haosu, gfischer]@wpi.edu

M. Zervas and C. Furlong are with Center for Holographic Studies and Laser micro-mechaTronics (CHSLT) and NanoEngineering, Science and Technology (NEST), Department of Mechanical Engineering, Worcester Polytechnic Institute, 100 Institute Road, Worcester, MA 01609, USA
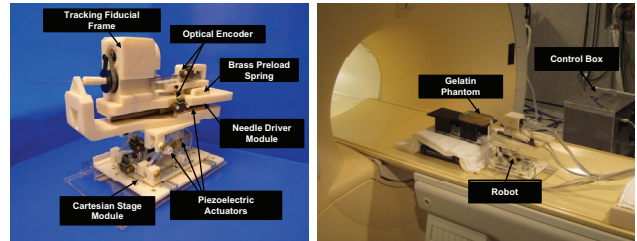
Fig. 1. (Left) Physical prototype of 6-DOF piezoelectric actuated needle placement robot consisting of needle driver module and Cartesian gross positioning module. The needle driver module provides $8cm$ insertion stroke, $5cm$ stylet retraction stroke and 40 revolutions per minute rotation speed. The Cartesian gross positioning module provides $8cm$ axial motion, $3cm$ elevation and $4cm$ lateral motion. (Right) The robot prototype in the bore of a 3T MRI scanner with a phantom.

of pneumatically actuated robotic devices [2]. Stoianovici *et al.* described a MRI-compatible pneumatic stepper motor and applied it to robotic brachytherapy seed placement [3]. Our previous work presented a pneumatic servo system and sliding mode control [4], [5]. Kokes *et al.* [6] reported a pneumatic needle driver system for radio frequency ablation of breast tumors. Song *et al.* [7] reported a pneumatically actuated modular robotic system with parallel mechanism.

Pneumatic actuation does have a low level of image interference, however the scalability, simplicity, size and inherent robustness of electromechanical systems present a clear advantage over pneumatically actuated systems. To this end, Chinzei *et al.* [8] developed a general-purpose robotic assistant with ultrasonic motors. Goldenberg *et al.* [9] presented targeting accuracy and MRI compatibility tests for a MRI-guided robot employing ultrasonic actuators for close-bore MRI scanners. Due to unacceptable signal noise from the motor, the motor was disabled during the scanning. Krieger *et al.* [10] recently designed a transrectal prostate robot actuated by piezoelectric motors with $40\%-60\%$ SNR reduction under motion.
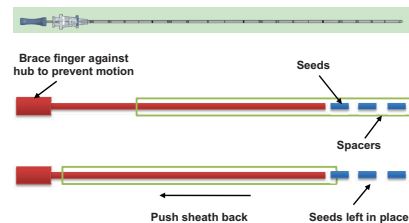

Fig. 2. (Top) Brachytherapy Needle from CP Medical, (bottom) schematic of preloaded needles: after insertion, the sheath is withdrawn over the stylet, leaving the seeds in the place (modified from [11]).

However, no prior work has investigated piezoelectric actuated robotic systems for needle steering under real-time high-field continuous MRI. With its many merits, in a transperineal manner which alleviates the requirement to perform the implant procedures in a different pose than used for preoperative imaging. Our ultimate overall goal is to develop a teleoperated needle placement system consists of a slave needle placement robot and a fiber optic force sensor to achieve prostate intervention under continuous high-field MRI. *Hence, the contributions of the paper are (1) the first demonstration of a 6-DOF needle placement robot with steering capability under real-time 3T MRI guidance with less than 2% SNR loss at full speed during imaging, and (2) opto-mechanical design of a high-resolution fiber optic force sensor to measure needle insertion force and render haptic display.*

This paper is organized as follows: Section II describes the system requirements and mechanism design including system architecture, robot structure and optical tracking frame. Section III presents the controller electrical design and system setup. Fiber optic sensing principle and opto-mechanical design are presented in Section IV. Phantom experiment in a 3T close MRI bore and sensor calibration are presented in Section V. Section VI concludes the paper with discussion and future work.

II. NEEDLE DRIVER MECHANISM DESIGN

A. System Concept and Specifications

Besides the MRI compatibility constraint, there are following design considerations:

1) Motion degree of freedom: 3-DOF motion needle driver and 3-DOF Cartesian gross positioning stage as shown in Fig. 1. A coarse to fine architecture decouples the motion and simplifies the kinematics, while guaranteeing high targeting accuracy. As shown in Fig. 2 top, the clinical 18Gauge needles for prostate brachytherapy have an inner stylet and hollow sheath. Radioactive seeds are pre-loaded with $5.5mm$ spacers between them before staring the surgery. During the insertion, one hand holds the cannula and the other hand brace against stylet hub to prevent relative motion. After insertion, the sheath is withdrawn over the stylet while leaving the seeds in place. To mimic the physician preload needle type brachytherapy procedure, the needle driver provides 1-DOF cannula rotation about its axis with 1-DOF translational insertion. Another 1-DOF of translational stylet motion is implemented to coordinate the motion with respect to the cannula. The rotation motion of the cannula may be used for bevel-based steering to limit deflection [12] or may be used for active cannula [13].

2) Operation in confined space: when the patient lies in the scanner bore with semilithotomy position, the lateral space between the legs is around $8cm$. To fit into this space, the width of the needle driver module has a wedge shape with $6cm$ front width ($10cm$ long) and $10cm$ back width ($25cm$ long).

3) Sterilization: only the plastic tip guide, collet, nut and guide sleeve have direct contact with the needle and are

removable and sterilizable.

B. System Architecture

Three-dimensional surgical navigation software 3D Slicer serves as a user interface with the robot. The navigation software is running on a Linux-based workstation in the scanner's console room. The system workflow follows a preoperative planning, optical frame registration, targeting and verification. OpenIGTLink [14] is used to exchange control, position, and image data. To perform dynamic global registration between the robot and scanner, a passive tracking the fiducial frame is integrated to the robot as shown in Fig. 3.

C. Universal Needle Clamping and Loading Mechanism

To design a needle driver that allows a large variety of standard needles to be used, a new clamping device rigidly connect the needle shaft to the driving motor mechanism is developed as shown in Fig. 3. It consists of three components made of ABS plastic: collet, collet nut and collet screw shaft. This structure is a collet mechanism and a hollow screw is twisted to fasten the collet thus rigidly locks the needle shaft on the clamping device. The clamping device is connected to the rotary motor through a timing belt. An eccentric pulley tensioner that is concentric with the rotary piezoelectric motor can freely adjust the distance between the motor and the clamping mechanism. The clamping device is generic in the sense that each collet can accommodate a wide range of standard medical needle diameters. The overall needle diameter range for three collets is from 25 Gauge ($0.5144mm$) to 16 Gauge ($1.651mm$). By this token, it can not only fasten brachytherapy needles but also biopsy needle or most other standard needles instead of designing some specific structure to hold the needle as those in [15]. The plastic needle guide with quick release mechanism, collet, nut and guide sleeve have direct contact with the needle and are low lost and disposable.
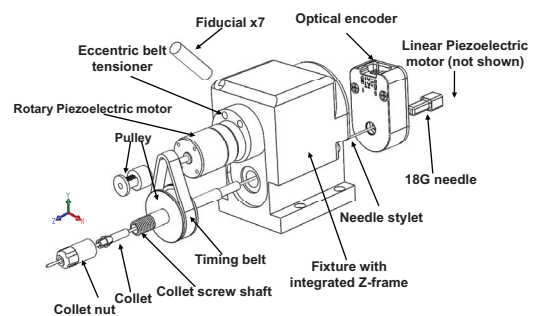

Fig. 3. A exploded view of the needle clamping mechanism, fiducial tracking frame and rotary motor fixture with timing belt tensioner.

Since the linear motor for controlling the inner stylet with respect to the outer cannula is collinear with the collet and shaft (Fig. 3), it is necessary to offset the shaft to manually load the needle. A brass spring preloaded mechanism (Fig. 1) is proposed which provides lateral passive motion freedom. The operator can pinch the mechanism and offset the top

motor fixture then load needle and lock with the needle clamping. This structure allows for easy, reliable and rapid loading of standard needles.

III. NEEDLE DRIVER ELECTRICAL DESIGN

A. Hardware Architecture

The PiezoMotor actuators (Uppsala, Sweden) chosen are non-harmonic piezoelectric motors, which have two advantages over a harmonic drive: the noise caused by the driving wave is much easier to suppress, and the motion produced by the motors is generally at a more desirable speed and torque. Optical encoders (US Digital, Vancouver, Washington) have been thoroughly tested in a 3T MRI scanner with satisfactory performance.

B. Piezoelectric Actuator Driver

Custom motor driver boards were developed [16], because commercially available hardware to drive piezoelectric motors do not consider the MRI frequency interference problem, and it is generally not possible to drive the motors with highly specific arbitrary waveforms without interference to the scanner. The driver is a 4 channel high power arbitrary waveform generator designed to run piezoelectric actuators. Waveform tables are loaded over USB or from SD card by a companion co-processor who is responsible for bootstrapping and provisioning the FPGA.

IV. FABRY-PEROT INTERFERENCE FIBER OPTIC SENSOR

It is reported in [17] that force sensing range for prostate brachytherapy is within 20 Newton and a resolution of 0.01 Newton is sufficient. Due to the loss of tactile feedback in a teleoperated needle placement robot [18], a 1-DOF fiber optic force sensor that measures *in vivo* needle insertion forces is proposed based on our previous effort [19] to render proprioception associated with brachytherapy.

A number of fiber optic force sensors for MRI applications based on light intensity modulation have been proposed [20], [21], to name a few. Due to the limited space in the robot design, there is a need to miniaturize the sensor while retain the sensing range and resolution requirement. Fiber Bragg Grating (FBG) sensors seem to be a viable solution. FBG directly correlate the wavelength of light and the change in the desired strain. If the fiber is strained from applied loads then these gratings will change accordingly and allow a different wavelength to be reflected back from the fiber. However, the costly optical source, FBG fibers and spectral analysis equipment present formidable application for medical instrumentation. Fabry-Perot interference (FPI) fiber optic sensor provides an amiable solution for high-resolution force sensing that only relies on simple interference pattern based voltage measurement.

A. Principle of Fabry-Perot based Fiber Optic Sensor

In a Fabry-Perot strain sensor, light propagates through a cavity containing semi-reflective mirrors. Some light and transmitted and some is reflected. As shown in the top of
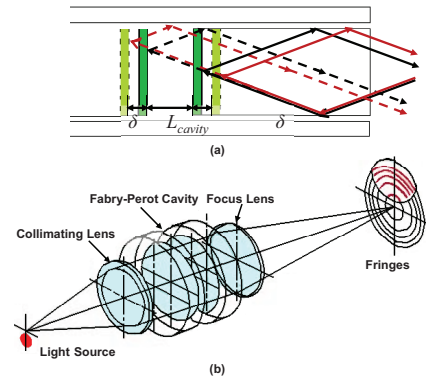

Fig. 4. Fabry-Perot sensing principle. (Top) light propagation in Fabry-Perot cavity, (bottom) resulting fringe pattern.

Fig. 4, the distance between the two fiber tips is generally on the order of nanometers and, depending on the gauge length (the active sensing region, defined as the distance between fusion welds). L_{cavity} is the original cavity length. δ is the change in the cavity length from a given load. The returning light interferes resulting in black and white bands known as fringes (Fig. 4 bottom) caused by destructive and constructive interference. The intensity of these fringes varies due to a change in the optical path length related to a change in cavity length when uni-axial force is applied.

This phenomenon can be quantified through the summation of two waves [22]. By multiplying the complex conjugate and applying Euler's identity, we obtain the following equation of reflected intensity at a given power for planar wave fronts:

$$I = A_1^2 + A_2^2 + 2A_1A_2 cos(\phi_1 - \phi_2) \quad (1)$$

with A_1 and A_2 representing the amplitude coefficients of the reflected signals. The above equation can be changed to represent only intensities by substituting $A_i^2 = I_i (i = 1, 2)$ and $\phi_1 - \phi_2 = \Delta\phi$ as

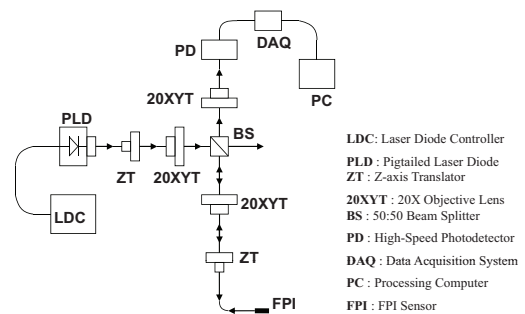$$I = I_1 + I_2 + 2\sqrt{I_1 I_2} cos\Delta\phi \quad (2)$$

Fig. 5. Schematic diagram of the opto-mechanical design to implement FPI sensor.

An FPI fiber optic strain sensor (FISO Technologies, Canada) was used to evaluate the systems resolution and

potential integration into the robot. The main component of the FPI is the sensing cavity, measuring $15.8\mu m$ wide. A glass capillary covering the sensing region is fusion welded to the fiber in two locations and encapsulates the sensor. There is an air gap of approximately $100.5\ \mu m$ wide. The total length of the FPI sensor, including the glass capillary, and bare fiber is approximately $20mm$. Besides immune to electromagnetic and RF signal and substantially cheaper than FBG, the advantages of this sensor includes: 1) static/dynamic response capability, 2) high sensitivity and resolution, 3) no interference due to cable bending and 4) robust to a large range of temperature variation ($-40°\sim250°$) due to air gap insulation to the sensing region.

B. Opto-mechanical Design

As depicted in Fig. 5, the opto-mechanical design of the prototype begins with a pigtailed laser diode (PLD) which emits light in the $830nm$ rand of the infrared line with a power of 1mW. This diode is controlled by a laser diode controller (LDC) (ITC-502, ThorLabs Inc, USA) which has a PID built in which helps stabilize the temperature and current of the diode when attached to laser cooler. The output of the pigtailed laser that exits the FC connector (FC) at the end of the sensor's fiber is connected to a Z axis translator (ZT). This Z axis translator helps focus the divergent light onto a $20X$ objective lens (Olympus, Japan) mounted to an $X-Y$ axis translator (20XYT). This collimated light is sent into a $50:50$ beam splitter cube (BS) (BS017, Thorlabs Inc, USA) where 50% of the light is split towards the FPI sensor and the other 50% is not used.

The light that is sent to the sensor is focused onto the $50\mu m$ core of the sensor's multi-mode fiber. This focusing is accomplished with the help of another $20X$ objective lens mounted to an $X-Y$ axis translator which focuses the light onto the fiber core which is able to adjust via a Z-axis translator which has the FPI fiber's ST connector (ST) attached to it. The light travels through the fiber and into the sensing cavity and then back reflects out the same optical axis it came in. This back reflected light passes through the $20X$ objective lens and is collimated into the beam splitter and once through the beam splitter the light is sent into the photodetector (PD) (DET10A, Thorlabs Inc, USA). The photodetector's output is digitized by a 16-bit data acquisition system (DAQ) (USB 6229-BNC, National Instruments, USA) and a processing computer (PC) is used to calculate the strain values.

C. Force Sensing Design

Due to negligible friction force between the needle and needle guide, the reaction forces between the mechanism (top plate) and the actuator drive rod is used to measure needle insertion force as shown in the top of Fig. 6. The beam to hold the actuator rod has a small $1.59mm$ groove to lay the sensor that would extend $30mm$ along its side where the FPI sensor could be embedded. The appropriate length was provided to ensure that the PVC fiber covering would be secured to the top plate and provide added durability
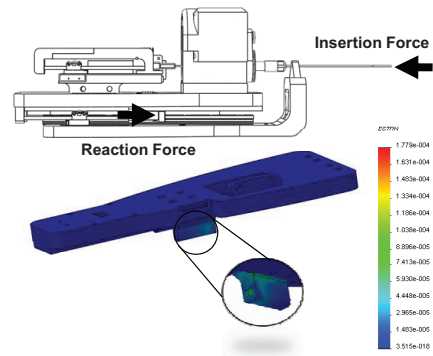

Fig. 6. (Top) needle insertion force measurement based on motor interaction force. (bottom) finite element analysis of ABS top plate under 10 Newton axial force.

to the sensor. Because each friction driven piezoelectric actuator can provides 12Newton force, the insertion translational motion is provided by two linear motors. In terms of the insertion force range, 10Newton interaction force is the maximum required for each sensor. The finite element analysis in Fig. 6 illustrates the maximum strain $100\mu\epsilon$ under 10 Newton axial force using ABS plastic material with a Young's Modulus of $2GPa$ and Poisson's ratio 0.34.

V. EXPERIMENTS AND RESULTS

To demonstrate the system MRI compatibility of this architecture and the designed piezoelectric driver, a series of MRI phantom tests were performed. The sensing capability of FPI sensor was also demonstrated by experiment.

A. MRI Compatibility Verification

The MRI compatibility of the needle placement robot was demonstrated in a Philips Achieva 3T system. The phantom employed in the experiment was a $12cm$ diameter plastic tube filled with a copper sulfate solution. The motor and encoder were placed immediately adjacent to the left side of the coil. The controller was placed approximately 3m from the scanner bore.
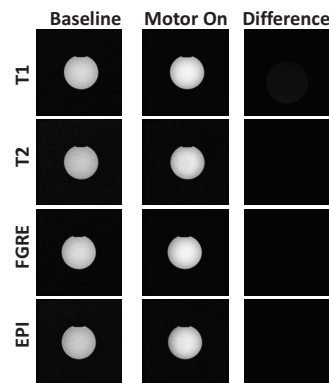

Fig. 7. Representative results showing the difference in images obtained of baseline and motor running conditions. Different with the results in [9] and [10], this demonstrates the real-time in situ needle steering capability.

Four imaging protocols were selected for evaluation of compatibility of the system: 1) diagnostic imaging T1-weighted fast gradient echo (T1 FGE/FFE), 2) diagnostic imaging T2-weighted fast spin echo (T2 FSE/TSE), 3) high-speed real-time imaging fast gradient echo (FGRE), and 4) functional imaging spin echo-planar imaging (SE EPI). All sequences were acquired with a slice thickness of $5mm$ and a number of excitations (NEX) of one. Three configurations were evaluated and used in the comparison: 1) baseline of the phantom only, 2) motor unpowered with controllers DC power supply turned on, 3) motor on and robot is in motion. Eight slices were acquired per imaging protocol for each configuration. Images obtained during motor operation in the scanner are subtracted from the baseline images, as shown in Fig. 7. For statistical analysis, SNR is utilized as the metric for evaluating MRI compatibility with baseline phantom image comparison [23]. Statistical analysis with a Tukey Multiple Comparison confirms that no pair shows significant signal degradation with a 95% confidence interval.
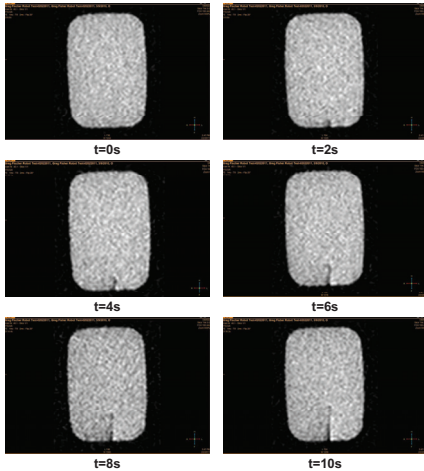

Fig. 8. Bevel tip needle insertion snapshots during 3T echo-planar imaging at 0.4 second interval.

B. Needle Insertion and Steering under Real-Time MRI-Guidance

A series of experiments are performed to evaluate the system performance for needle insertion and steering capability under real-time 3T MRI-guidance.

The first test is the dynamic needle insertion. Gelatin ($12cm$ length, $9cm$ width and $5cm$ thickness) is utilized as a tissue phantom for in vitro needle steering. The gelatin was mixed with boiling water at a ratio of 1 to 1. A $22Gauge$ medical needle ($0.82mm$ outer diameter) with $45°$ bevel tip is used for steering test. Functional imaging spin echo-planar imaging (field of view $240mm$, echo time $1ms$, repetition time $2ms$, flip angle $20°$) is utilized to monitor the real-time needle motion. This imaging protocol provides approximately $2Hz$ update rates. Needle insertion motion without needle rotation is controlled by closed-loop optical encoder feedback with proportional-integral-derivative controller. Fig. 8 depicts six bevel tip needle insertion snapshots during 3T

echo-planar imaging at 0.4 second interval. The needle shaft and tip trajectories are clearly visualized in the phantom image without major interference during robot motion.

In the second test, the same $22Gauge$ medical needle is used to demonstrate the steering capability with MRI visualization. The bevel tip is rotated toward left before insertion. T2-weighted fast spin echo (field of view $240mm$, echo time $90ms$, repetition time $3000ms$, flip angle $90°$) illustrates the final needle shape and tip position. The same procedure is repeated for bevel right before insertion and the results are shown in Fig. 9. There is no visually identifiable interference during needle robot controlled insertion.

All the three tests demonstrate the *in situ* piezoelectric actuation capability in 3T MRI, thus enables real-time needle steering. The compatibility performance and dynamic needle insertion result is significant comparing with the ones in [9] and [10], which have $40\% - 60\%$ SNR reduction under motion and must interleave motion with imaging.
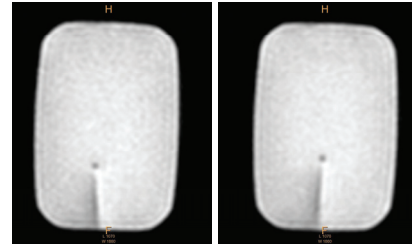

Fig. 9. Bevel tip needle steering image in 3T MRI. (Left) bevel left needle insertion and (right) bevel right needle insertion .

C. Fiber Optic Force Sensor Calibration

Calibration was performed by attaching the FPI to a manufactured ABS cantilever beam. Strain on the beam was calculated in terms of the applied force F:

$$\epsilon_{xx} = \frac{12FLc}{bt^3E} \qquad (3)$$

where L is the length of the beam, c is the distance from the center of the beam along the y-direction, b is the width of the base, t is the thickness, and E is Young's modulus.

In order to calibrate the FPI, the relationship between the intensity of light at the output and the strain was derived. A hanger system was employed at the end of the cantilever beam to statically apply the load in increments of the 5 grams.

Recall in equation 2, the change in phase $\Delta\phi$ of the intensity equation is equal to the wave number $\frac{2\pi}{\lambda}$, multiplied by the length of the sensing cavity region and the strain in the x-direction:

$$\Delta\phi = \frac{2\pi(\epsilon_{xx}L_{cavity})}{\lambda} \qquad (4)$$

This value for the change in phase was substituted into intensity equation and it is now possible to predict the output intensity of light as a function of the induced strain:

$$I = 2I_0[1 + cos(\frac{2\pi(\epsilon_{xx}L_{cavity})}{\lambda})] \qquad (5)$$
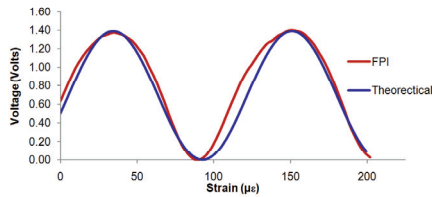
Fig. 10. Calibration results showing voltage versus strain of the FPI sensor together with the theoretical model.

The calibrated system can be seen in the voltage-strain graph shown in Fig. 10. The theoretically predicted relationship is superimposed in the figure. The output voltage follows a sinusoidal pattern that repeats over an increasing applied force. The discrepancy between the measurement and theoretical model is due to the ambient light disturbance to the opto-mechanical prototype which is not shielded during experiment. A gage factor of $47.48mv/\mu\epsilon$ was calculated and when using a 16 bit data acquisition system.

VI. CONCLUSION

This paper presents the design of a MRI compatible piezoelectric actuated 6-DOF robot integrated with a high-resolution fiber optic force sensor for image guided brachytherapy. The MRI compatibility test of the robot and the calibration result of the sensor demonstrate the real-time piezoelectric actuation and sensing capability. The next step of this work will focus on packaging the opto-mechanical system and attain robust and portable interface with the robot controller. Needle steering with the proposed robot prototype will be performed to demonstrate the targeting accuracy in live tissue. Sensor hysteresis, fluctuation and drift would be further investigated with multiple needle insertions and retractions.

VII. ACKNOWLEDGMENTS

REFERENCES

[1] N. Abolhassani, R. Patel, and M. Moallem, "Needle insertion into soft tissue: A survey," *Medical Engineering and Physics*, vol. 29, no. 4, pp. 413 – 431, 2007.

[2] G. S. Fischer, A. Krieger, I. I. Iordachita, C. Csoma, L. L. Whitcomb, and G. Fichtinger, "MRI Compatibility of Robot Actuation Techniques – A Comparative Study," *Int Conf Med Image Comput Comput Assist Interv*, Sept. 2008.

[3] D. Stoianovici, D. Song, D. Petrisor, D. Ursu, D. Mazilu, M. Muntener, M. Mutener, M. Schar, and A. Patriciu, "MRI Stealth robot for prostate interventions.," *Minim Invasive Ther Allied Technol*, vol. 16, no. 4, pp. 241–248, 2007.

[4] Y. Wang, H. Su, K. Harrington, and G. Fischer, "Sliding mode Control of piezoelectric valve regulated pneumatic actuator for MRI-compatible robotic intervention," in *ASME Dynamic Systems and Control Conference - DSCC 2010*, (Cambridge, MA, USA), 2010.

[5] H. Su and G. S. Fischer, "High-field MRI-Compatible needle placement robots for prostate interventions: pneumatic and piezoelectric approaches," in *Advances in Robotics and Virtual Reality* (T. Gulrez and A. Hassanien, eds.), Springer-Verlag, 2011.

[6] R. Kokes, K. Lister, R. Gullapalli, B. Zhang, A. MacMillan, H. Richard, and J. Desai, "Towards a teleoperated needle driver robot with haptic feedback for RFA of breast tumors under continuous MRI," *Medical Image Analysis*, vol. 13, no. 3, pp. 445 – 55, 2009/06/.

[7] S.-E. Song, N. Cho, G. Fischer, N. Hata, C. Tempany, G. Fichtinger, and I. Iordachita, "Development of a pneumatic robot for MRI-guided transperineal prostate biopsy and brachytherapy: New approaches," in *Robotics and Automation (ICRA), 2010 IEEE International Conference on*, pp. 2580 –2585, May 2010.

[8] K. Chinzei and K. Miller, "Towards MRI guided surgical manipulator.," *Med Sci Monit*, vol. 7, no. 1, pp. 153–163, 2001.

[9] A. Goldenberg, J. Trachtenberg, W. Kucharczyk, Y. Yi, M. Haider, L. Ma, R. Weersink, and C. Raoufi, "Robotic system for closed-bore MRI-guided prostatic interventions," *Mechatronics, IEEE/ASME Transactions on*, vol. 13, pp. 374 –379, Jun. 2008.

[10] A. Krieger, I. Iordachita, S.-E. Song, N. Cho, P. Guion, G. Fichtinger, and L. Whitcomb, "Development and preliminary evaluation of an actuated MRI-compatible robotic device for MRI-guided prostate intervention," pp. 1066 –1073, May 2010.

[11] K. Wallner, J. Blasko, and M. Dattoli, *Prostate Brachytherapy Made Complicated*. Smart Medicine Press, 2007.

[12] M. Mahvash and P. Dupont, "Fast needle insertion to minimize tissue deformation and damage," in *Proc. IEEE International Conference on Robotics and Automation ICRA 2009*, pp. 3097 – 3102, 2009.

[13] D. Rucker and R. Webster, "Mechanics of bending, torsion, and variable precurvature in multi-tube active cannulas," in *Proc. IEEE International Conference on Robotics and Automation ICRA 2009*, pp. 2533 – 7, 2009.

[14] J. Tokuda and G. Fischer, "OpenIGTLink: an open network protocol for image-guided therapy environment," *Int J Med Robot*, vol. 5, pp. 423–34, Dec. 2009.

[15] H. S. Bassan, R. V. Patel, and M. Moallem, "A novel manipulator for percutaneous needle insertion: Design and experimentation," *IEEE/ASME Transactions on Mechatronics*, vol. 14, no. 6, pp. 746 – 761, 2009.

[16] G. Cole, K. Harrington, H. Su, A. Camilo, J. Pilitsis, and G. Fischer, "Closed-Loop Actuated Surgical System Utilizing Real-Time In-Situ MRI Guidance," in *12th International Symposium on Experimental Robotics - ISER 2010*, (New Delhi and Agra, India), Dec 2010.

[17] Y. Yu, T. Podder, Y. Zhang, W. S. Ng, V. Misic, J. Sherman, L. Fu, D. Fuller, E. Messing, D. Rubens, J. Strang, and R. Brasacchio, "Robot-assisted prostate brachytherapy," Medical Image Computing and Computer-Assisted Intervention - MICCAI 2006, (Berlin, Germany), pp. 41–9, Springer-Verlag, 2006.

[18] H. Su, W. Shang, G. Cole, K. Harrington, and F. S. Gregory, "Haptic system design for MRI-guided needle based prostate brachytherapy," IEEE Haptics Symposium 2010, (Boston, MA, USA), IEEE, 2010.

[19] H. Su, M. Zervas, C. Furlong, and G. Fischer, "A miniature MRI-compatible fiber-optic force sensor utilizing fabry-perot interferometer," in *SEM Annual Conference and Exposition on Experimental and Applied Mechanics*, (Uncasville, CT, USA), 2011.

[20] H. Su and G. Fischer, "A 3-axis optical force/torque sensor for prostate needle placement in magnetic resonance imaging environments," 2nd Annual IEEE International Conference on Technologies for Practical Robot Applications, (Boston, MA, USA), pp. 5–9, IEEE, 2009.

[21] P. Polygerinos, P. Puangmali, T. Schaeffter, R. Razavi, L. Seneviratne, and K. Althoefer, "Novel miniature MRI-compatible fiber-optic force sensor for cardiac catheterization procedures," in *Robotics and Automation (ICRA), 2010 IEEE International Conference on*, pp. 2598 –2603, May 2010.

[22] T. K. Gangopadhyay, "Prospects for fibre bragg gratings and fabry-perot interferometers in fibre-optic vibration sensing," *Sensors and Actuators A: Physical*, vol. 113, no. 1, pp. 20 – 38, 2004.

[23] Y. Wang, G. Cole, H. Su, J. Pilitsis, and G. Fischer, "MRI compatibility evaluation of a piezoelectric actuator system for a neural interventional robot," in *Annual Conference of IEEE Engineering in Medicine and Biology Society*, (Minneapolis, MN), pp. 6072–6075, 2009.